Versão do arquivo anexado / Version of attached file:

Versão do Editor / Published Version

Mais informações no site da editora / Further information on publisher's website:

https://www.osapublishing.org/oe/abstract.cfm?uri=oe-26-9-11238

DOI: 10.1364/OE.26.011238

Direitos autorais / Publisher's copyright statement:

Low-aberration beamline optics for synchrotron infrared nanospectroscopy

RAUL O. FREITAS,[1,*] CHRISTOPH DENEKE,[2,3] FRANCISCO C. B. MAIA,[1] HELTON G. MEDEIROS,[1,4] THIERRY MORENO,[5] PAUL DUMAS,[5] YVES PETROFF,[1] AND HARRY WESTFAHL[1]

[1] *Brazilian Synchrotron Light Laboratory (LNLS), Brazilian Center for Research in Energy and Materials (CNPEM), 13083-970, Campinas, Sao Paulo, Brazil*
[2] *Brazilian Nanotechnology National Laboratory (LNNano), Brazilian Center for Research in Energy and Materials (CNPEM), 13083-970, Campinas, Sao Paulo, Brazil*
[3] *Universidade Estadual de Campinas (Unicamp), Instituto de Física Gleb Wataghin, 13083-859, Campinas, Sao Paulo, Brazil*
[4] *Universidade Federal do Rio de Janeiro (UFRJ), 25245-390, Xerem, Rio de Janeiro, Brazil*
[5] *SOLEIL Synchrotron, Gif Sur Yvette Cedex, 91192, France*
*raul.freitas@lnls.br

Abstract: Synchrotron infrared nanospectroscopy is a recently developed technique that enables new possibilities in the broadband chemical analysis of materials in the nanoscale, far beyond the diffraction limit in this frequency domain. Synchrotron infrared ports have exploited mainly the high brightness advantage provided by electron storage rings across the whole infrared range. However, optical aberrations in the beam produced by the source depth of bending magnet emission at large angles prevent infrared nanospectroscopy to reach its maximum capability. In this work we present a low-aberration optical layout specially designed and constructed for a dedicated synchrotron infrared nanospectroscopy beamline. We report excellent agreement between simulated beam profiles (from standard wave propagation and raytracing optics simulations) with experimental measurements. We report an important improvement in the infrared nanospectroscopy experiment related to the improved beamline optics. Finally, we demonstrate the performance of the nanospectroscopy endstation by measuring a hyperspectral image of a polar material and we evaluate the setup sensitivity by measuring ultra-thin polymer films down to 6 nm thick.

OCIS codes: (180.4243) Near-field microscopy; (220.1000) Aberration compensation.

References and links

1. R. Henderson and P. N. T. Unwin, "Three-dimensional model of purple membrane obtained by electron microscopy," Nature, **257**, 28–32 (1975).
2. J. Dubochet and A. W. McDowall, "Vitrification of Pure Water for Electron Microscopy," Journal of Microscopy **124**, 3–4 (1981).
3. R. K. Agrawal, P. Penczek, R. A. Grassucci, Y. Li, A. Leith, K. H. Nierhaus and J. Frank, "Direct visualization of A-, P-, and E-site transfer RNAs in the Escherichia coli ribosome," Science **271**, 1000–1002 (1996).
4. S. W. Hell and M. Kroug, "Ground-state-depletion fluorescence microscopy: a concept for breaking the diffraciton resolution limit. Applied Physics B: Lasers and Optics," **60**, 495–497 (1995).
5. E. Betzig, "Proposed method for molecular optical imaging," Optics Letters **20**, 237–239 (1995).
6. R. M. Dickson, A. B. Cubitt, R. Tsien and W. E. Moerner, "On/off blinking and switching behaviour of single molecules of green fluorescent protein," Nature **388**, 355–358 (1997).
7. T. A. Klar, S. Jakobs, M. Dyba, A. Egner and S. W. Hell, "Fluorescence microscopy with diffraction resolution barrier broken by stimulated emission," Proceedings of the National Academy of Sciences **97**, 8206–8210 (2000).
8. E. Betzig, G. H. Patterson, R. Sougrat, O. W. Lindwasser, S. Olenych, J. S. Bonifacino, M. W. Davidson, J. Lippincott-Schwartz and H. F. Hess, "Imaging intracellular fluorescent proteins at nanometer resolution," Science **313**, 1642–1645 (2006).
9. D. A. Shapiro, Y. S. Yu, T. Tyliszczak, J. Cabana, R. Celestre, W. Chao, K. Kaznatcheev, A. L. D. Kilcoyne, F. Maia, S. Marchesini, Y. S. Meng, T. Warwick, L. L. Yang and H. A. Padmore, "Chemical composition mapping with nanometre resolution by soft X-ray microscopy," Nature Photonics **8**, 765–769 (2014).

10. P. R. Griffiths and J. A. de Haseth, *Fourier Transform Infrared Spectrometry. Chemical Analysis: A Series of Monographs on Analytical Chemistry and Its Applications* (John Wiley & Sons, 2007).

11. M. J. Nasse, M. J. Walsh, E. C. Mattson, R. Reininger, A. Kajdacsy-Balla, V. Macias, R. Bhargava and C. J. Hirschmugl, "High-resolution Fourier-transform infrared chemical imaging with multiple synchrotron beams," Nature Methods **8**, 413–416 (2011).

12. M. J. Hackett, F. Borondics, D. Brown, C. Hirschmugl, S. E. Smith, P. G. Paterson, H. Nichol, I. J. Pickering and G. N. George, "Subcellular biochemical investigation of purkinje neurons using synchrotron radiation fourier transform infrared spectroscopic imaging with a focal plane array detector," ACS Chemical Neuroscience **4**, 1071–1080 (2013).

13. E. Giorgini, G. Gioacchini, S. Sabbatini, C. Conti, L. Vaccari, A. Borini, O. Carnevali and G. Tosi, "Vibrational characterization of female gametes: a comparative study," The Analyst **139**, 5049–5060 (2014).

14. K. Goda and B. Jalali, "Dispersive Fourier transformation for fast continuous single-shot measurements," Nature Photonics **7**, 102–112 (2013).

15. U. Schade, E. Ritter, P. Hegemann, E. F. Aziz and K. P. Hofmann, "Concept for a single-shot mid-infrared spectrometer using synchrotron radiation," Vibrational Spectroscopy **75**, 190–195 (2014).

16. E. Ritter, L. Puskar, F. J. Bartl, E. F. Aziz, P. Hegemann and U. Schade, "Time-resolved infrared spectroscopic techniques as applied to channelrhodopsin," Frontiers in Molecular Biosciences **2**, 38 (2015).

17. D. K. Spaulding, G. Weck, P. Loubeyre, F. Datchi, P. Dumas and M. Hanfland, "Pressure-induced chemistry in a nitrogen-hydrogen host?guest structure." Nature Communications **5**, 5739 (2014).

18. C. Pépin, P. Loubeyre, F. Occelli and P. Dumas, "Synthesis of lithium polyhydrides above 130 GPa at 300 K," Proceedings of the National Academy of Sciences **112**, 7673–7676 (2015).

19. S. Kawata and Y. Inouye, "Scanning probe optical microscopy using a metallic probe tip," Ultramicroscopy **57**, 313–317 (1995).

20. F. Zenhausern, Y. Martin and H. K. Wickramasinghe, "Scanning interferometric apertureless microscopy: optical imaging at 10 angstrom resolution," Science **269**, 1083–1085 (1995).

21. B. Knoll and F. Keilmann, "Near-field probing of vibrational absorption for chemical microscopy," Nature **399**, 7–10 (1999).

22. F. Keilmann and R. Hillenbrand, "Near-field microscopy by elastic light scattering from a tip," Philosophical Transactions. Series A, Mathematical, Physical, and Engineering Sciences **362**, 787–805 (2004).

23. F. Huth, M. Schnell, J. Wittborn, N. Ocelic and R. Hillenbrand, "Infrared-spectroscopic nanoimaging with a thermal source," Nature Materials **10**, 352–356 (2011).

24. S. Gamage, Z. Li, V. S. Yakovlev, C. Lewis, H. Wang, S. B. Cronin and Y. Abate, "Nanoscopy of Black Phosphorus Degradation," Advanced Materials Interfaces **3**, 1–6 (2016).

25. H. Amrania, L. Drummond, R. C. Coombes, S. Shousha, K. Weir, W. Hart, I. Carter and C. C. Phillips, "New IR imaging modalities for cancer detection and for intra-cell chemical mapping with a sub-diffraction mid-IR," Faraday Discussions **187**, 539–553 (2016).

26. R. Wiens, C. R. Findlay, S. G. Baldwin, L. Kreplak, J. M. Lee, P. Veres and K. M. Gough, "High spatial resolution (1.1 μm and 20 nm) FTIR polarization contrast imaging reveals pre-rupture disorder in damaged tendon," Faraday Discussions **187**, 555–573 (2016).

27. F. Huth, A. Govyadinov, S. Amarie, W. Nuansing, F. Keilmann and R. Hillenbrand, "Nano-FTIR absorption spectroscopy of molecular fingerprints at 20 nm spatial resolution," Nano Letters **12**, 3973–3978 (2012).

28. A. A. Govyadinov, I. Amenabar, F. Huth, P. S. Carney and R. Hillenbrand, "Quantitative measurement of local infrared absorption and dielectric function with tip-enhanced near-field microscopy," Journal of Physical Chemistry Letters **4**, 1526–1531 (2013).

29. C. M. Johnson and M. Böhmler, "Nano-FTIR microscopy and spectroscopy studies of atmospheric corrosion with a spatial resolution of 20nm," Corrosion Science **108**, 60–65 (2016).

30. I. Amenabar, S. Poly, M. Goikoetxea, W. Nuansing, P. Lasch and R. Hillenbrand, "Hyperspectral infrared nanoimaging of organic samples based on Fourier transform infrared nanospectroscopy," Nature Communications **8**, 14402 (2017).

31. M. Wagner, D. S. Jakob, S. Horne, H. Mittel, S. Osechinskiy, C. Phillips, G. C. Walker, C. Su and X. G. Xu, "Ultrabroadband Nanospectroscopy with a Laser-Driven Plasma Source," ACS Photonics, **Article ASAP** (2018).

32. Y. Ikemoto, M. Ishikawa, S. Nakashima, H. Okamura, Y. Haruyama, S. Matsui, T. Moriwaki and T. Kinoshita, "Development of scattering near-field optical microspectroscopy apparatus using an infrared synchrotron radiation source," Optics Communications **285**, 2212–2217 (2012).

33. P. Hermann, A. Hoehl, P. Patoka, F. Huth, E. Rühl and G. Ulm, "Near-field imaging and nano-Fourier-transform infrared spectroscopy using broadband synchrotron radiation," Optics Express **21**, 2913–2919 (2013).

34. H. A. Bechtel, E. A. Muller, R. L. Olmon, M. C. Martin and M. B. Raschke, "Ultrabroadband infrared nanospectroscopic imaging," Proceedings of the National Academy of Sciences **111**, 7191–7196 (2014).

35. B. Pollard, F. C. B. Maia, M. B Raschke and R. O. Freitas, "Infrared Vibrational Nanospectroscopy by Self-Referenced Interferometry," Nano Letters **16**, 55–61 (2016).

36. W. D. Duncan, G. P. Williams, B. Hill and B. National, "Infrared synchrotron radiation from electron storage rings," Applied Optics **22**, 2914–2923 (1983).

37. P. Hermann, A. Hoehl, G. Ulrich, C. Fleischmann, A. Hermelink, B. Kästner, P. Patoka, A. Hornemann, B. Beckhoff, E. Rühl and G. Ulm, "Characterization of semiconductor materials using synchrotron radiation-based near-field infrared microscopy and nano-FTIR spectroscopy," Optics Express **22**, 17948–17958 (2014).

38. P. Patoka, G. Ulrich, E. A. Nguyen, L. Bartels, P. A. Dowben, V. Turkowski, T. S. Rahman, P. Hermann, B. Kästner, A. Hoehl, G. Ulm and E. Rühl, "Nanoscale plasmonic phenomena in CVD-grown MoS 2 monolayer revealed by ultra-broadband synchrotron radiation based nano-FTIR spectroscopy and near-field microscopy," Optics Express **24**, 1154–1164 (2016).

39. I. D. Barcelos, A. R. Cadore, L. C. Campos, A. Malachias, K. Watanabe, T. Taniguchi, F. C. B. Maia, R. Freitas and C. Deneke, "Graphene/h-BN plasmon-phonon coupling and plasmon delocalization observed by infrared nano-spectroscopy," Nanoscale **7**, 11620–11625 (2015).

40. Z. Shi, H. A. Bechtel, S. Berweger, Y. Sun, B. Zeng, C. Jin, M. C. Martin, M. B. Raschke and H. Chang and F. Wang, "Amplitude- and Phase-Resolved Nanospectral Imaging of Phonon Polaritons in Hexagonal Boron Nitride," ACS Photonics **2**, 790–796 (2015).

41. D. Grasseschi, D. Bahamon, F. C. B. Maia, A. H. C. Neto, R. O. Freitas and C. J. S. de Matos, "Oxygen impact on the electronic and vibrational properties of black phosphorus probed by synchrotron infrared nanospectroscopy," 2D Materials **4**, aa8210 (2017).

42. G. Dominguez, A. S. Mcleod, Z. Gainsforth, P. Kelly, H. A. Bechtel, F. Keilmann, A. Westphal, M. Thiemens and D. N. Basov, "Nanoscale infrared spectroscopy as a non-destructive probe of extraterrestrial samples." Nature Communications **5**, 5445 (2014).

43. C. -Y. Wu, W. J. Wolf, Y. Levartovsky, H. A. Bechtel, M. C. Martin, F. D. Toste and E. Gross, "High-spatial-resolution mapping of catalytic reactions on single particles," Nature **541**, 511–515 (2017).

44. O. Chubar and P. Elleaume, "Accurate And Efficient Computation Of Synchrotron Radiation In The Near Field Region," Proceedings of the EPAC98 Conference, 1177–1179(1998).

45. T. Moreno and M. Idir, "SPOTX a ray tracing software for X-ray optics," J. Phys. IV France **11**, 527–531 (2001).

46. G. Geloni, V. Kocharyan, E. Saldin, E. Schneidmiller and M. Yurkov, "Theory of edge radiation. Part I: Foundations and basic applications," Nuclear Instruments and Methods in Physics Research, Section A: Accelerators, Spectrometers, Detectors and Associated Equipment **605**, 409–429 (2009).

47. T. Moreno, H. Westfahl, R. O. Freitas, Y. Petroff and P. Dumas, "Optical layouts for large infrared beamline opening angles," Journal of Physics: Conference Series **425**, 142003 (2013).

48. T. Moreno, "Compact IR synchrotron beamline design," Journal of Synchrotron Radiation **24**, 1–6 (2017).

49. L. M. Zhang, G. O. Andreev, Z. Fei, A. S. McLeod, G. Dominguez, M. Thiemens, A. H. Castro-Neto, D. N. Basov and M. M. Fogler, "Near-field spectroscopy of silicon dioxide thin films," Physical Review B **85**, 1–8 (2012).

50. C. B. Walsh and E. I. Franses, "Ultrathin PMMA films spin-coated from toluene solutions," Thin Solid Films **429**, 71–76 (2003).

1. Introduction

The most of the functionalities and fundamental properties of materials are intrinsically related to their chemical structure. In the last few years, the need for spatially-resolved chemical analysis has driven a rapid development of ultra-microscopy techniques such as cryo-electron microscopy [1–3], super-resolution fluorescence microscopy [4–8] and also soft X-rays nanoscopy via coherent diffraction imaging [9], among others. Despite the exceptional resolution power for imaging in the nano to the atomic scales, these techniques commonly require sophisticated sample preparation procedures such as thickness control, beam damage monitoring, operation in vacuum and labeling for chemical identification. On the other hand and with simpler experimental requirements, Fourier Transform Infrared spectroscopy (FTIR) [10] is long recognized for its chemical specificity in the mid-infrared range (mid-IR), allowing for non-destructive label-free molecular identification and imaging. However, due to the Abbe diffraction limit, FTIR spatial resolution is typically not better than few microns. By benefiting from sources with high brightness in the mid-IR range, such as synchrotron IR sources, IR spectro-microscopy (μ-FTIR) can achieve sub-micron resolution when operating in full-field imaging mode combined with focal plane array (FPA) detectors [11–13]. Moreover, advanced experiments such as dispersive time-resolved IR spectroscopy [14–16] and μ-FTIR under high pressure conditions [17,18] are currently feasible due to the high signal-to-noise ratio (SNR) delivered by IR ports at synchrotron facilities. In spite of the robustness and high sensitivity of synchrotron μ-FTIR, many open questions related to the nano-heterogeneity of materials cannot be addressed.

IR scattering Scanning Near-Field Optical Microscopy (IR s-SNOM) is a technique able to measure optical properties of materials beyond the classical diffraction limit of light [19–21]. In IR s-SNOM, atomic force microscopy (AFM) is combined with IR microscopy for providing surface morphology and opto-vibrational response in a single experiment. Free-space incident

radiation is confined into sub-diffractional volumes via antenna effect driven by an AFM metallic tip [22]. These confined fields are spatially constrained to the surface of the tip apex which shapes an IR probe with dimensions comparable to the tip radius, defining a typical optical resolution of 25 nm [22]. This confined fields interact with the sample surface in standard AFM tapping mode, generating a back-scattered wave with the time signature of the tip dynamics. The asymmetric detection scheme of the s-SNOM allows measuring both amplitude and phase of the tip scattered wave. Far-field background suppression is done via lock-in detection with demodulation in higher harmonics of the tip resonance frequency [22]. Therefore, the technique is able to measure not only scattering but also absorption properties of materials, a key requirement for the nanoscale chemical analysis. A proof-of-concept using a black body source [23] has paved the way for the application of IR s-SNOM as a broadband IR nanospectroscopy tool, however, the low brightness and lack of polarization of classical thermal sources prevent their use in studies involving materials with low scattering power, such as organics. Since then, IR s-SNOM has evolved in phase with the developments of new IR sources as Quantum Cascade Lasers (QCLs) for narrow band imaging [24–26], broadband tunable Difference Frequency Generation lasers (DGFs) [27–30], laser-driven plasma sources [31] and IR synchrotron radiation [32–35]. Especially when using synchrotron sources, IR s-SNOM can achieve unprecedented molecular specificity due to the high spectral irradiance of synchrotron IR radiation (up to 1000 times brighter than thermal sources [36]). Hence, a variety of research fronts have applied synchrotron IR s-SNOM (nano-FTIR) as a decisive tool in studies involving semiconductor physics [37], two-dimensional (2D) materials and nanophotonics [38–41], nano-chemistry of extraterrestrial fragments [42], biomaterials [34], nano-catalysis [43] and nano-optics [35].

In this work we present the performance of nano-FTIR operating with synchrotron IR from a beamline with specially designed optics that highly minimizes the typical source depth aberration of large horizontal and vertical IR extraction ports. Nano-FTIR relies on condensing far-field broadband IR onto a nano-antenna. Therefore, the attained beamline optics optimization leads to improved focus and wave front quality at the tip-sample stage, which are key elements for the nano-FTIR performance. Here we describe the details of this special beamline optics and test it in the nano-FTIR experiment. We demonstrate a comprehensive nano-optical characterization of a standard polar material, including nano-resolved chemical images reconstructed from a nano-FTIR hyperspectral map. Finally, we tested the nano-FTIR sensitivity up to the limit of few-molecules thick polymer film.

2. Light source and beamline optics

Synchrotron IR radiation has been extracted from a 1.67 T dipole installed in the Brazilian Synchrotron Light Laboratory (LNLS), a 1.37 GeV second generation storage ring that operates in decay mode from 250 mA to 120 mA (~12 hours shifts). Figure 1(a) depicts the beamline optical layout with the 5 mirrors (M1 to M5) responsible for collection, focusing and collimation of the extracted bending magnet (BM) radiation. The original dipole vacuum chamber was modified in order to allow large collection angles (80 mrad × 30 mrad, horizontal × vertical), a modification that is essential for maximizing the IR extraction at long (several microns) wavelengths (Fig. 1(b)). In Figure 1(c), the special designed conical mirror (M2) is shown. Figure 1(d) illustrates the BM spectral irradiance from ultra-violet (UV) to the far-IR (100 nm to 100 μm) which is 3 to 4 orders higher than classical blackbody IR emission [36]. All mirrors are gold coated (200 nm Au on aluminum substrate) and are installed in ultra-high vacuum (UHV) environment. The first optical element (M1) is a flat mirror that spatially separates the IR-VIS radiation from the high energy white beam. No active cooling was required for M1 since a 360 mm × 7 mm horizontal slot allows for by-passing more than 98% of the beam heat load.

Figures 2(a)-2(c) and Figs. 2(d)-2(f) show 10 μm IR intensity maps at M1 simulated by the wave propagation software Synchrotron Radiation Workshop (SRW) [44] and by the raytracing
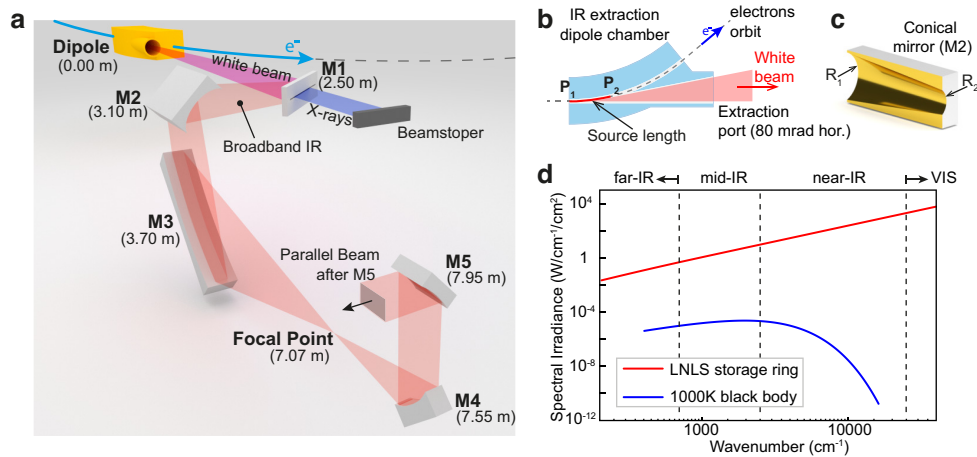
Fig. 1. (a) Beamline primary optics for extraction, focusing and collimation of the BM radiation. (b) Scheme of the custom designed dipole vacuum chamber for IR extraction. The electrons trajectory in the sight of the port defines the source length. (c) Cartoon of the conical mirror M2 which is able to compensate for source depth aberrations. (d) SRW calculated spectral irradiance of the IR1 extraction port compared to blackbody emission from a 1000K globar simulated via XOP.

program spotX [45], respectively. Both simulations converge to similar levels of flux density ($\sim 2 \times 10^9$ ph/s/0.1%bw/mm^2) except by the right side of the SRW simulated map (Fig. 2(a)) that shows additional intensity (interference fringes) from edge emission [46]. The main aberrations expected in IR extraction ports arise from source shape, *i. e.*, source depth produces vertical distortions while the circular source shape generates horizontal coma aberrations. In order to compensate for the source depth aberration, a conical mirror in tangential reflection (M2, Fig. 1(c)) has been calculated and designed with radii gradient from R1 (5018 mm) to R2 (4826 mm), as proposed in [47, 48]. The radii R1 to R2 compensate the longitudinal path from P1 to P2 illustrated in Fig. 1(b). A long cylindrical mirror (M3, R=4986 mm), located at 3.7 m from the source origin, compensates the circular source shape caused by the electrons trajectory, hence, removing coma aberrations. The combination of M2 and M3 respectively suppress vertical and horizontal aberrations producing a sharp secondary source few centimeters downstream from a diamond window. A Si charge-coupled device (CCD) camera (Manta G-146, Allied Vision Technologies GmbH) with a 980 nm bandpass filter (FB980-10, Thorlabs Inc.) was used for imaging the beam cross-section near the designed focal plane. The beam converged vertically and horizontally (smaller beam waist) to the longitudinal position 7.07±0.02 m from the source origin.

Figures 3(a) and 3(b) show spotX simulation and measured images of the beam focal point (FP) cross-section at 7.07 m for λ=980 nm. Vertical and horizontal profiles (Figs. 3(c) and 3(d)) indicate FP dimensions of 1100 μm × 400 μm (FWHM), respectively, with good agreement between simulated and measured profiles. An additional intensity spread is observed bellow the FP in Fig. 3(b) and it is possibly related to the edge radiation (not taken into account by spotX) that comes together with the BM continuous emission. Simulations at λ=10 μm (data not shown) indicate FP dimensions of 1100 μm × 500 μm (FWHM). In this energy, only the short axis (vertical plane of the storage ring) has increased due to the energy dependency of the BM emission. Downstream from the FP, two cylindrical mirrors are set to collimate the radiation to be further propagated into the experimental station. M4 (R=1361 mm) collimates the vertical component of the beam while M5 (R=2493 mm) collimates horizontally. Figures
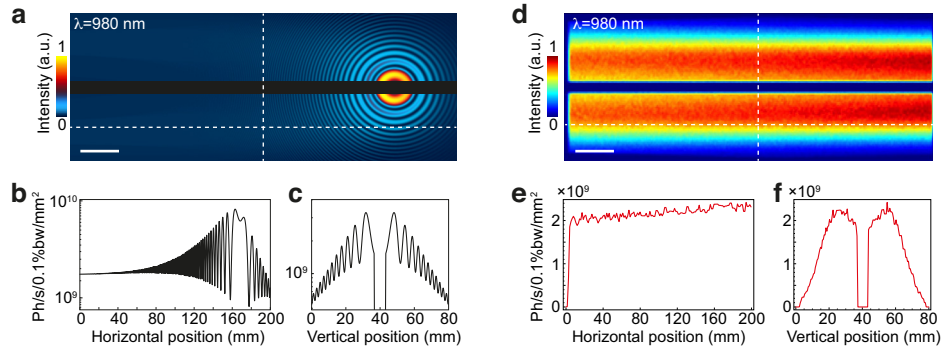
Fig. 2. SRW (a–c) and spotX (d–f) simulations of the beam cross-section at M1 for λ=980 nm. Scale bars in (a,b) represent 20 mm.
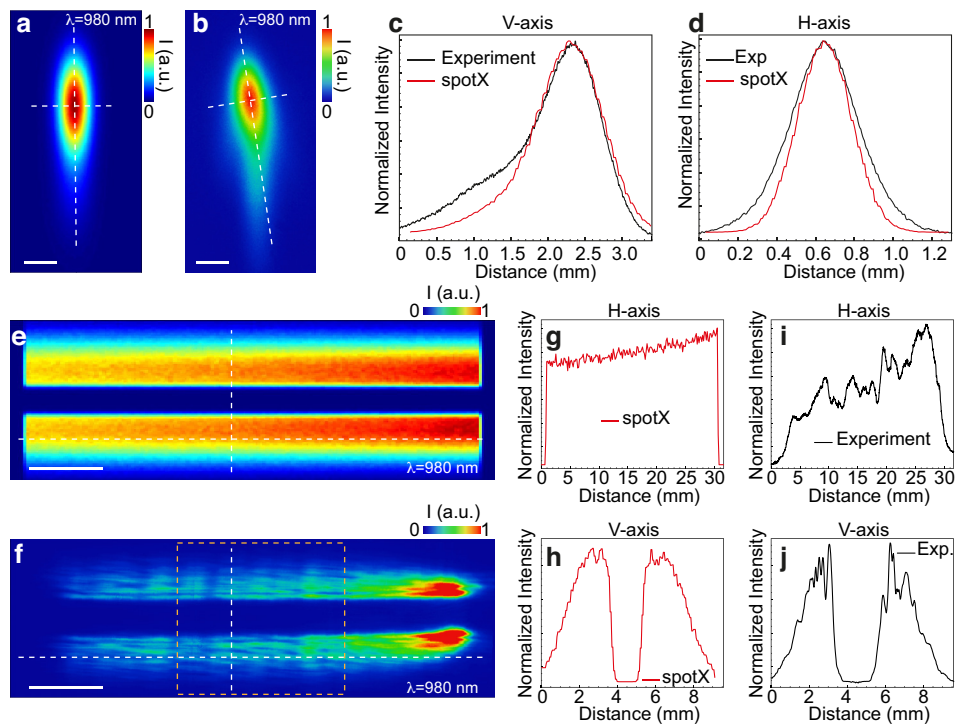

Fig. 3. Focal point intensity cross-sections (a) simulated by spotX and (b) measured at ~7 m from the origin for λ=980 nm. (c,d) Intensity profiles along the white dashed lines in (a,b). Simulated (e) and measured (f) intensity cross-sections of the collimated beam right after M5. The yellow dashed rectangle in (f) indicates the portion of the beam used in the nano-FTIR experiment. Simulated (g,h) and measured (i,j) intensity profiles of the collimated beam taken along the white dashed lines in (e,f). White scale bars represent 500 μm (a,b) and 5 mm (e,f).

3(e) and 3(f) show spotX simulated and CCD measured cross-sections of the beam right after M5 for 980 nm wavelength. Figures 3(g) and 3(h) show simulated intensity profiles along the white dashed lines indicated in Fig. 3(e). Experimental curves in Figs. 3(i) and 3(j) present measured intensity profiles along the white dashed lines indicated in Fig. 3(f). The experimental profiles in Figs. 3(i) and 3(j) indicate beam dimensions of 24.0 mm × 6.5 mm (H×V), with reasonable agreement with the results from spotX raytracing. As predicted in the SRW simulation of the source (Fig. 2(b)), an extra intensity is measured on the right area of the collimated beam cross-section which is associated to the edge emission. The spotX simulations do not take into account wave interferences effects, therefore, do not consider the edge emission. We measured the beam divergence after M5, which resulted in ~1.0 mrad by ~0.3 mrad in horizontal and vertical directions, respectively for λ=980 nm. The simulated divergence values from spotX gives ~1.8 mrad by ~0.3 mrad, which are in relatively good agreement with the experiments. The total power of collimated beam (from 2 μm to 20 μm) was measured as 2.17 mW (full beam including continuous and edge emission) and 0.54 mW (beam entering the nano-FTIR instrument).

3. Nano-FTIR experiment

From the beamline primary optics depicted in Fig. 1(a), a parallel IR beam is propagated to the endstation dedicated to ultra-broadband IR nanospectroscopy (IR1 endstation).A diagram of the IR1 endstation is presented in Fig. 4(a). Entering a commercial s-SNOM instrument (NeaSNOM, Neaspec GmbH), the beam is reduced by slits down to ~10×10 mm^2 (dashed square in Fig. 3(f)) in order to match the acceptance of the microscope. It is further divided into the two arms of a Michelson interferometer by a parallel ZnSe beamsplitter. At the s-SNOM arm, the beam is focused onto an AFM metallic tip (Arrow NCPt, NanoWorld AG) by a 0.45 NA off-axis parabolic mirror. In this configuration, the parabolic optics is also used to collect the backscattered photons generated by the tip-sample near-field optical interaction. AFM operates in tapping mode (Ω defined as tip frequency in the range of few hundreds of kHz), which introduces a time signature to the near-field optical interaction. This operation mode is an essential feature for far-field background suppression as well as for reaching ultimate optical resolution comparable to the tip radius ($\simeq R_{tip}$=25 nm) [22]. All nano-FTIR data presented in this work were measured via 2nd harmonic (2Ω) demodulation. The sample is mounted on a standard 3D piezo electric stage (PZT stage) for automatic vertical approaching and for in-plane mapping (AFM topography) of up to 100×100 μm^2 with minimum steps of 5 nm. On the other interferometer arm, a flat Au coated reference mirror is mounted on a linear PZT stage (P.629.1 PIHera, Physik Instrumente GmbH & Co. KG), that modulates the optical path difference (OPD) of the reference far-field beam. The maximum spectral resolution is 3.3 cm^{-1} corresponding to a travel of 1.5 mm (3 mm OPD) of the reference mirror. The beams from both arms, after recombination at the beamsplitter, propagate up to a Mercury Cadmium Telluride detector (MCT KLD-0.25 , Kolmar Technologies Inc.). The signal from the MCT is introduced into the NeaSNOM built-in lock-in amplifier together with the AFM photodiode signal (reference signal), in order to measure the amplitude and the phase of the scattering response [22]. Figure 4(b) shows a spotX raytracing simulation of the cross-section of the focal point at the tip-sample stage for 10 μm wavelength. In the simulation, we considered a focusing paraboloid at 10.5 m from the source (downstream M5), 25 mm focal length, 60° orientation focusing downwards and 12×11 mm^2 beam acceptance. These simulation parameters are based on the actual condenser installed in the nano-FTIR instrument. The total flux calculated for λ=10μm at the tip is 4.3×10^{12} ph/s/0.1%bw. Figures 4(c)-4(d) present the intensity profiles along the dashed white lines indicated in Figure 4(b). The black profiles indicate 40 μm and 9 μm FWHM in the horizontal and vertical directions, respectively. The red dashed curve in Figure 4(d) illustrate the intensity profile along the vertical plane of a simulated focal point at the tip for a standard beamline optics. In that case, we simulated M2 and M3 as a typical toroidal mirror and the flux at the tip was estimated to be ~8.2×10^{11} ph/s/0.1%bw. In a direct comparison, the
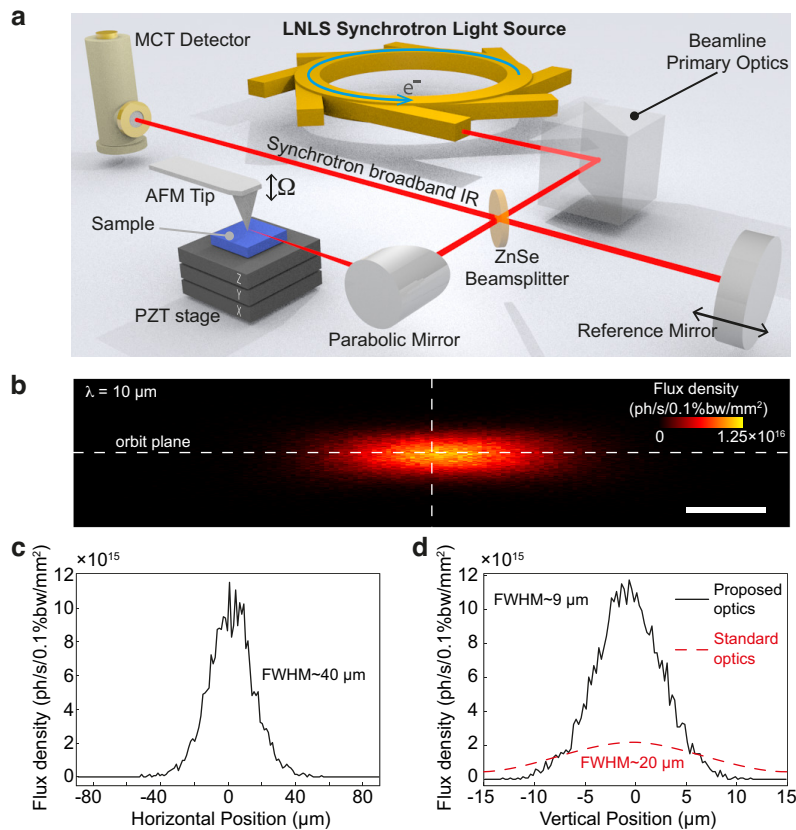
Fig. 4. (a) Scheme of the nano-FTIR experiment at LNLS. (b) spotX simulation of the focal point at the AFM tip at 10 μm wavelength. (c-d) Intensity profiles along the horizontal and vertical dashed lines marked in (b). Black solid profiles in (c-d) indicate the spotX simulation using the proposed beamline optics (conical-cylindrical shapes for mirrors M2-M3) and red dashed profile in (d) indicate the focal point at the tip when using standard beamline optics (toroidal shape for M2-M3). In the actual experiment, a periscope is used in order to align the long axis of the focus with the tip shaft. Scale bar in (b) represents 20 μm.

vertical aberration correction brought by the proposed optics provides ~5 times more flux at the tip compared to a standard beamline layout. As the antenna effect is direct related to the electric field arriving at the tip, we estimate an improvement in the s-SNOM signal proportional to the increase in IR flux density at the tip.

Figure 5 shows a nano-FTIR spectrum (black curve) from Au/Si substrate and a far-field background spectrum (blue curve) taken at the same experimental conditions. The spectra were taken using 6.25 cm^{-1} spectral resolution, 2048 points, 20 ms integration time, 30 scans (black curve) and 10 scans (blue curve). All spectra were measured in air environment (relative humidity 40–50%) and were normalized by their maximum value. Both spectra show maxima around 1000 cm^{-1} and then decay in similar slope as the MCT responsivity. However, after 3000 cm^{-1} the far-field spectrum displays an intensity increase while the near-field signal keeps decreasing up to 6000 cm^{-1}. The decay of the near-field signal above 3000 cm^{-1} comes from the lower antenna efficiency of the used AFM tips for wavelengths shorter than 3 μm. Spectral features seen in both far and near-field spectra come from the water rotational bands and CO_2 from the environment. The features observed next to 800 cm^{-1}, 950 cm^{-1}, 1100 cm^{-1} and 1260 cm^{-1} are related to tips
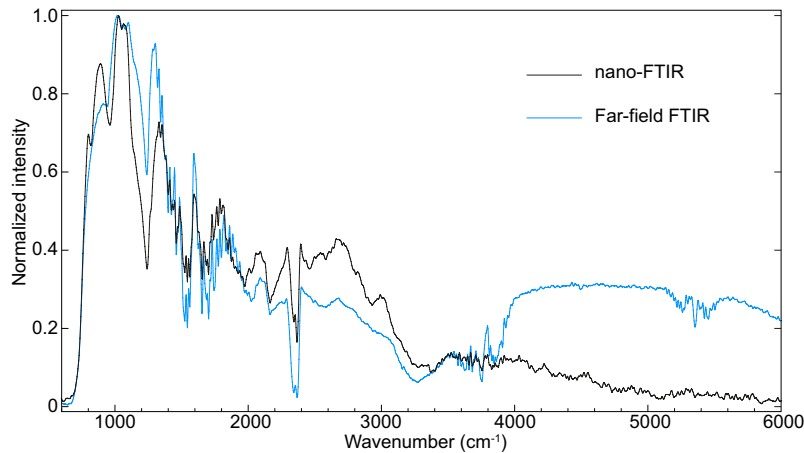
Fig. 5. Nano-FTIR (black curve), far-field FTIR (blue curve) standard reference spectra from a gold substrate in the IR1 setup. Scale bar in (b) represents 20 μm.

contamination by polydimethylsiloxane (PDMS), a common gel present in commercial AFM tips packing.

4. Nano-FTIR of optical and molecular materials

A complete nano-optical characterization of a SiO_2/Si micro-pattern (HS-100MG, Budget Sensors) is presented in Figure 6. Broadband s-SNOM 2D mapping with 200×40 pixels^2 in an area of 10×2 μm^2 featuring 100 nm high SiO_2 micro-stripes is presented in Fig. 6(a). Each pixel of 50×50 nm^2 shows an integrated signal that corresponds to the broadband s-SNOM amplitude (broadband image). The contrast between SiO_2 and Si regions is related to the different refractive indexes of those materials across the energy range of the experiment. AFM topography was measured simultaneously with the broadband image revealing the 100 nm high SiO_2 steps (bottom of Fig. 6(b)). Figure 6(b) shows a spatio-spectral map (linescan) along the horizontal dashed line in (a). The set of 80 spectra (125 nm spaced, 6.25 cm^{-1} spectral resolution) reveals the distinct spectral response between Si and SiO_2. While Si has a flat IR response in the range, SiO_2 presents a broad amplitude peak around 1100 cm^{-1} corresponding to the surface phonon-polaritons (SPhP) activity stimulated by the near-field interaction [49]. This type of measurement is essential for the study of opto-chemical transitions and interfaces in nanomaterials. Once the heterogeneity is revealed by both broadband imaging and spectral linescan, we collected a point spectrum at the center of the SiO_2 stripe (see red dot in the inset cartoon in Fig. 6(c)), which reveals the expected lineshape for the SiO_2 SPhP as shown in Fig. 6(c).

An ultimate step for nano-FTIR is the ability of measuring nanoscale chemical images. In this modality, each pixel of an image contains a full spectrum (hyperspectral image) and hence a 4D dataset is measured (X, Y, Intensity, Frequency). By selecting a particular frequency (or integrate in a range of frequencies), the hyperspectral image allows for reconstruction of energy-selective intensity maps (or narrowband maps). Figures 6(d) and 6(e) show narrowband maps extracted from a full hyperspectral image of the SiO_2/Si stripes with 80×8 pixels^2 in an area of 10×2 μm^2. Each pixel has a full spectrum with 1024 points, 6.0 ms integration time per point, 12.5 cm^{-1} spectral resolution. Figure 6(d) shows a narrowband map in which each pixel is the integrated s-SNOM amplitude from 1040 cm^{-1} to 1160 cm^{-1}. This spectral range, defined in Fig. 6(c) as "ON", is inside the SiO_2 SPhP peak and, hence, Fig. 6(d) highlights the presence of SiO_2 that has stronger response than the Si in the range. On the other hand, Fig. 6(e) shows inverted contrast as the integrated range, defined as "OFF" in Fig. 6(c), is outside the SiO_2 SPhP resonance where the
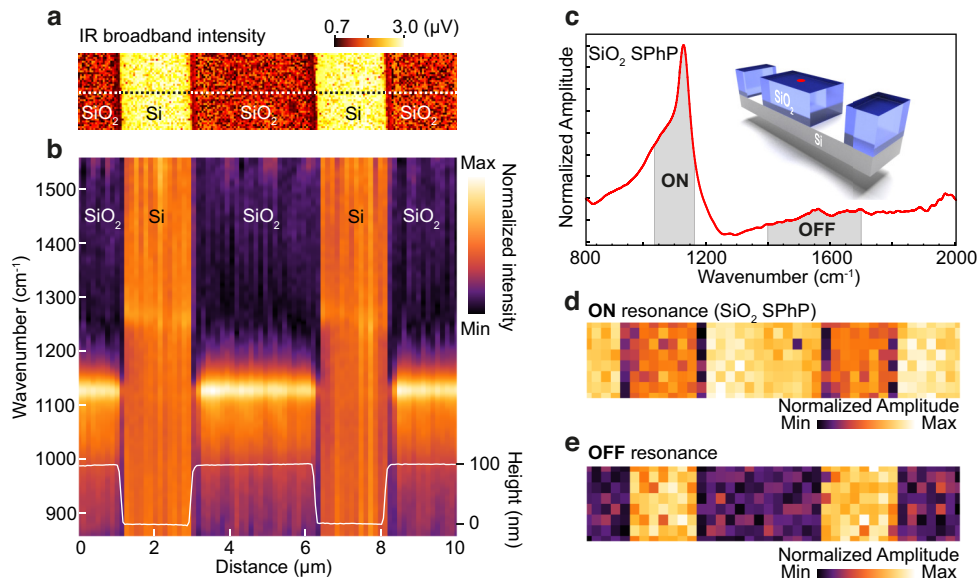
Fig. 6. (a) Broadband IR image of a SiO_2/Si AFM micro-standard. (b) Spectral linescan along the horizontal dashed line in (a). AFM topography indicated by the white line at the bottom of (b). (c) Point nano-FTIR spectrum taken at the center of the SiO_2 step (red dot in the inset 3D cartoon of the sample). Energy-selective nano-FTIR maps for integrated frequency ranges (d) inside the SiO_2 SPhP peak and for frequencies outside the SiO_2 phonon resonance. Maps extracted from a full hyperspectral map of the sample.

Si response is stronger than SiO_2. Hyperspectral imaging is very time-consuming, and represents a challenging experiment for nano-FTIR. For weak-oscillators materials, such as organics, large integration periods are needed and hyperspectral images can take up to few hours. In those cases, mechanical and spectral drifts can be critical for defining the spatial resolution of the technique. Recently, hyperspectral imaging using a DFG tunable laser of organic systems reveals the power of this imaging modality but still requires sophisticated imaging post-processing procedures for compensating mechanical and spectral drifts [30]. However, for materials with strong vibrational response, such as polar crystals, hyperspectral imaging can be afforded in shorter acquisition periods avoiding the detrimental contributions of instabilities. All data presented in Fig. 6 were normalized by an Au reference spectrum for suppressing the influence of environment absorption bands.

For a sensitivity test in organic materials, we prepared a series of thin films of Poly(methyl methacrylate) (PMMA) deposited on Au/Si substrates following the procedure in Ref. [50]. Figure 7 shows a detailed comparison between nano-FTIR and Attenuated Total Reflection FTIR (ATR-FTIR) measurements for those films. Figure 7(a) show nano-FTIR spectra of PMMA/Au films with thicknesses 312, 120, 45, 25, 11, 6 and 3 nm. In this case, the spectrum of the imaginary part of the s-SNOM signal is presented as the nano-FTIR absorbance which is compatible to far-field FTIR absorption [27, 28]. Each spectrum is an average of 40 accumulations of scans of 2048 points, 10 cm^{-1} spectral resolution and 20 ms integration time per point. Molecular absorption lines of PMMA are around 1145 cm^{-1} (CH_2 bending), 1190 cm^{-1} (C−O−C bending), 1265 cm^{-1} and 1240 cm^{-1} (C−C−O stretching), and 1730 cm^{-1} (C=O stretching), which are observed in most of the nano-FTIR spectra in Fig. 7(a). The inverted peaks observed bellow 1300 cm^{-1} are related to PDMS contamination of the tips during the commercial packaging. Figure 7(b) shows a direct spectral comparison between nano-FTIR (black curve) and ATR-FTIR (blue curve)
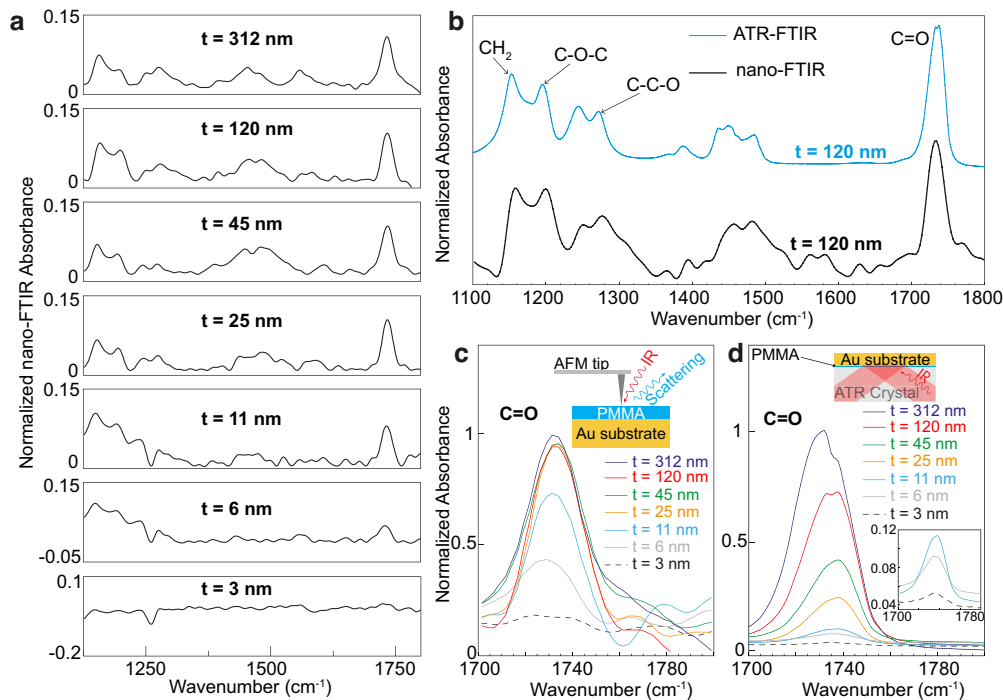
Fig. 7. (a) Nano-FTIR imaginary spectra of PMMA films with thicknesses from 312 nm to 3 nm. (b) Spectral comparison between far-field FTIR (blue curve) and nano-FTIR (black curve) measured from a 120 nm PMMA/Au film. Zoom on the spectral absorbance of the C=O functional group for several films thicknesses measured with (c) nano-FTIR and (d) ATR-FTIR. Bottom inset in (d) shows ATR-FTIR for thicknesses 3, 6 and 11 nm.

of a 120 nm thick PMMA film with excellent agreement between the two techniques. ATR-FTIR spectra were measured in a bench-top FTIR spectrometer (Spectrum Two with a diamond crystal ATR module, Perkin Elmer) set with 3.3 cm^{-1} spectral resolution and 32 accumulations for signal averaging of each individual spectrum. Figures 7(c) and 7(d) show in detail the C=O vibrational mode probed by nano-FTIR and ATR-FTIR, respectively, for all PMMA films. For the nano-FTIR measurement, it is possible to resolve the C=O peak for all thicknesses except for the 3 nm PMMA film, when the polymer vibrational activity is close to the noise level. This could be related to the fact that the 3 nm PMMA deposition do not produces a homogeneous layer but a set of ultra-thin separated domains (AFM data not shown). Figure 7(d) shows in detail the PMMA carbonyl vibrational resonance for all film thicknesses measured by ATR-FTIR in an area of 2×2 mm^2 of film. For the far-field experiment, all films present reasonably good SNR and are clearly noticed above the noise level. It is important to note that the ATR-FTIR absorbance scales almost linearly with the thicknesses of the films whereas the nano-FTIR absorbance do not follow the same trend. In the later, the presence of the Au substrate plays a key role in the technique sensitivity. As the polymer film thickness is reduced, a smaller number of oscillators contribute to the nano-FTIR absorbance. On the other hand, as the the gap tip-substrate is reduced, the stronger is the dipole-dipole interaction between the metallic tip and its mirror image in the Au substrate and, hence, the higher is the enhancement in the overall nano-FTIR signal, including the local molecular response of the polymer film. This explains the similar absorbance strength in nano-FTIR for the PMMA films with thicknesses 312, 120, 45 and 25 nm. Comparing directly the sensitivity of nano-FTIR and ATR-FTIR, the far-field technique presented SNR in the order

of 10^3 to 10^5 going from the thinner to the thicker PMMA films, while the nano-FTIR performed with SNR from 4 to 10. However, while the ATR probed an area of $\sim 4 \times 10^{12}$ nm^2, the nano-FTIR interaction takes place in an area of $\sim 6 \times 10^2$ nm^2, what means a factor of 10^{10} less molecules compared to ATR. These results reveal an outstanding molecular sensitivity of the nano-FTIR that is up to 10^6 higher than standard FTIR.

5. Conclusion

We have presented the performance of a nano-FTIR endstation that uses IR synchrotron radiation from a low-aberration beamline optics. The special design of our optics allows for correcting aberrations related to the source depth intrinsic to large extraction angles for IR synchrotron ports. Beam profiles measured at the focal point and after the collimation mirrors are in excellent agreement with wave and raytracing optics simulations. The optimized wave front of our beam has important consequences on the sensitivity of the nano-FTIR experiment that requires highly parallel beams for an improved focusing. We estimate a factor of 5 improvement in IR flux density at the tip comparing the new proposed optical layout to conventional IR beamline optics. The improvement in the nano-FTIR performance is understood to be proportional to the flux density increase. Measuring a SiO$_2$/Si micro-pattern, our setup was able to record a full hyperspectral nanoscale image, demonstrating the possibility of reconstruction of narrowband images using synchrotron s-SNOM. Moreover, we have evaluated the sensitivity of the setup in the analysis of ultra-thin organic films with thicknesses down to 6 nm. In summary, we have demonstrated that the sub-diffractional confinement driven by the s-SNOM antenna induces an outstanding enhancement in sensitivity, which allowed nano-FTIR to chemically characterize volumes $\sim 10^{10}$ smaller than the volumes probed by standard FTIR. The aberration-corrected optics developed for the beamline has been crucial for achieving the presented performances and the optical design represents a template for advanced IR imaging and spectroscopy endstations at synchrotron facilities, including the new class of machines based on multi-bend-achromat (MBA) lattices. Following the same concept presented here, a new optical layout is being planned for IR extraction from the new 4th generation storage ring in construction in Brazil, the SIRIUS lightsource, whose operation starts in 2019.

Disclosures

The authors declare that there are no conflicts of interest related to this article.